Charge Transfer from Methylammonium Lead Iodide Perovskite to Organic Transport Materials

Efficiencies, Transfer Rates, and Interfacial Recombination

Hutter, Eline M.; Hofman, Jan Jaap; Petrus, Michiel L.; Moes, Michiel; Abellón, Ruben D.; Docampo, Pablo; Savenije, Tom J.

DOI
10.1002/aenm.201602349

Publication date
2017

Document Version
Final published version

Published in
Advanced Energy Materials

Charge Transfer from Methylammonium Lead Iodide Perovskite to Organic Transport Materials: Efficiencies, Transfer Rates, and Interfacial Recombination

Eline M. Hutter, Jan-Jaap Hofman, Michiel L. Petrus, Michiel Moes, Ruben D. Abellón, Pablo Docampo, and Tom J. Savenije**

Perovskite-based photovoltaics have been rapidly developed, with record power conversion efficiencies now exceeding 22%. In order to rationally design efficient and stable perovskite solar cells, it is important to understand not only charge trapping and recombination events, but also processes occurring at the perovskite/transport material (TM) interface, such as charge transfer and interfacial recombination. In this work, time-resolved microwave conductivity measurements are performed to investigate these interfacial processes for methylammonium lead iodide and various state-of-the-art organic TMs. A global kinetic model is developed, which accurately describes both the dynamics of excess charges in the perovskite layer and transfer to charge-specific TMs. The authors conclude that for state-of-the-art materials, such as Spiro-OMeTAD and PCBM, the charge extraction efficiency is not significantly affected by intra-band gap traps for trap densities under 10^{15} cm^{-3}. Finally, the transfer rates to C60, PCBM, EDOT-OMeTPA, and Spiro-OMeTAD are sufficient to outcompete second order recombination under excitation densities representative for illumination by AM1.5.

1. Introduction

Solar cells employing metal halide perovskites as light absorbers have undergone a tremendous development over the past years, resulting in photovoltaic devices with record efficiencies exceeding 22%.[1–3] The impressive progress in device efficiency is mainly due to (i) optimizing experimental procedures to obtain perovskite materials with improved crystallinity, (ii) adjusting the perovskite composition, and (iii) investigating different transport materials. However, it remains a major challenge to eliminate the hysteresis in the photovoltaic current–voltage scans, thereby stabilizing perovskite-based solar cells. Recently, it was shown that hysteresis in perovskite-based solar cells is highly dependent on the choice of transport materials (TMs), suggesting that device performance is limited by charge accumulation at the interfaces.[4,5] Hence, better understanding of the perovskite/TM interfaces is critical for rational design of stable perovskite-based solar cells with minimum hysteresis and improved device lifetimes.

Interestingly, in contrast to the substantial progress that has been made in understanding the dynamics of photogenerated charges in the photo-active metal halide perovskite,[6,7] there are only a handful of reports investigating the kinetics of charge transfer from perovskite to charge-specific TMs.[8–12] We have previously proposed that injection of charges can be in competition with recombination pathways in the perovskite layer, in particular if the perovskite is unintentionally doped.[9] Other groups have extracted transfer rates[8] or yields[13] from global analysis of spectroscopic data. However, a quantitative description accounting both for the dynamics of charges in the perovskite itself and the transfer to charge-specific electrodes is still lacking.

In this work, we use time-resolved microwave conductivity (TRMC) measurements to reveal the charge carrier transfer and recombination pathways in bilayer systems of thin methylammonium lead iodide ($MAPbI_3$) films and charge-selective TMs. First, we prepared smooth, homogeneous $MAPbI_3$ layers using sequential physical vapor deposition (PVD).[14–16] Via this route, multiple $MAPbI_3$ films with identical optoelectronic properties can be made, which enables for direct comparison between different samples. Then, various organic electrodes were spin coated on top of the $MAPbI_3$ films, so that we could compare the photophysical processes in a bilayer to those in a neat perovskite.[9] The frequently used hole transporting materials (HTMs) Spiro-OMeTAD, H101[17] and the recently reported low-cost alternative EDOT-OMeTPA[18] were investigated. Similarly, state-of-the-art [6,6]-phenyl-C_{61}-butyric acid methyl ester (PCBM) and C60 were compared to less commonly used electron transport materials (ETMs) such as indene-C_{60} bis-adduct (ICBA)[19] and bis-adduct of PCBM (bis-PCBM).

E. M. Hutter, J.-J. Hofman, M. Moes,
R. D. Abellón, Dr. T. J. Savenije
Opto-Electronic Materials Section
Department of Chemical Engineering
Delft University of Technology
van der Maasweg 9, 2629 HZ, Delft, The Netherlands
E-mail: E.M.Hutter@tudelft.nl; T.J.Savenije@tudelft.nl
Dr. M. L. Petrus, Dr. P. Docampo[+]
Department of Chemistry and Center for NanoScience (CeNS)
LMU Munich
Butenandtstraße 5-13, 81377 Munich, Germany
[+]Present address: School of Electrical and Electronic Engineering, Newcastle University, Merz Court, NE1 7RU Newcastle upon Tyne, UK

DOI: 10.1002/aenm.201602349

Interestingly, we find that on the timescale of our TRMC experiment, charge transfer of electrons or holes occurs independently of excitation wavelength and illumination side, indicating that this process is not limited by charge diffusion in perovskite films with thicknesses of a few hundred nanometers. We introduce a global kinetic model that implements charge carrier generation, various recombination pathways in the perovskite layers and in addition, the transfer rates to charge-selective TMs. First, the dynamic parameters, including mobilities and rate constants for band-to-band recombination and trapping, are revealed for the neat perovskite layer, as previously described.[20,21] After depositing the TM layer, the same set of kinetic parameters plus an additional rate constant is used to describe the transfer of charges. Hence, we find the rates of charge transfer and interfacial recombination for a number of different organic TMs. Additionally, this model enables us to separate the electron and hole mobilities and to deduce the charge collection efficiency as function of charge carrier density (i.e., illumination intensity). We find that at low concentrations, charge transfer can be in competition with charge immobilization due to the presence of traps, whereas second order recombination in the perovskite dominates over extraction at higher concentrations. Most importantly, these results demonstrate that transfer of charges is optimized when the transfer rates exceed the trapping rates, which is the case for e.g., Spiro-OMeTAD and PCBM. These results pave the way for rational design of perovskite-based solar cells with balanced extraction of charges, which are essential for avoiding accumulation of charges at one of the electrodes.

2. Results and Discussion

To study the transfer of charges from $MAPbI_3$ to various organic TMs, the charge carrier dynamics in neat perovskite films were directly compared to bilayer systems. The different types of sample configurations are schematically shown in **Figure 1**. A short (3.5 ns full width at half maximum) laser pulse is used to excite the samples though the quartz substrate, thereby generating free charges in the $MAPbI_3$ layer. As previously reported, these charges decay over time by trap-assisted and/or second order electron–hole recombination.[20,22] When an ETM (or HTM) is deposited on top of the $MAPbI_3$, electrons (holes) are extracted and consequently, these can recombine via the interface with holes (electrons) that remained in the $MAPbI_3$.

Using $MAPbI_3$ layers with identical optoelectronic properties, the charge carrier dynamics and transfer to the electrodes was investigated quantitatively. The initial location of charges was manipulated by varying the excitation wavelength. **Figure 2**a shows the charge carrier generation profile in $MAPbI_3$ for excitation wavelengths of 300, 600, and 780 nm, calculated using the experimentally determined absorption coefficients α (see Figure S1 in the Supporting Information). At λ = 300 nm, the penetration depth ($1/\alpha$) of light is only 30 nm and hence, photo-excitation is concentrated close to the illuminated surface. On the other hand, at λ = 780 nm, the lower absorption coefficient results in a diluted, more homogeneous excitation profile. Figure 2b shows the normalized photoconductance ΔG in a thin (≈200 nm) vapor-deposited $MAPbI_3$ film (see Figure S2 to S4 in the Supporting Information)[14–16,23] as function of time after pulsed illumination (10^{10} absorbed photons cm^{-2} per pulse), recorded using the TRMC technique.[24] Given that ΔG provides a measure for the concentration of free mobile charges, its initial rise is due to charge generation by the laser pulse, whereas its reduction over time can be directly related to immobilization of charges by e.g., trapping or recombination. As shown in Figure 2b, the signal has reduced to half its initial value within 200 ns for an initial charge carrier concentration of 5×10^{14} cm^{-3}. Interestingly, this is independent of the excitation wavelength λ. Similar TRMC results were obtained for excitation from the front side (i.e., through the organic layer) and from the back side (see Figure S5 in the Supporting Information). Thus, the results in Figure 2b,c and Figure S5 in the Supporting Information show that the timescale for recombination does not depend on the initial distribution of charges, which indicates that transport occurs on a much faster timescale than recombination.

To gain more insight in the charge carrier dynamics in $MAPbI_3$ and the charge collection by TM layers, we deposited Spiro-OMeTAD on top of the perovskite and repeated the TRMC measurements. The samples were excited through the quartz substrate and thus, in this case, varying the excitation wavelength changes the distance of charge carriers to the MAPbI3/Spiro-OMeTAD interface. The change in conductance is given by

$$\frac{\Delta P(t)}{P} = -K\Delta G(t) \quad (1)$$

Then, the product of the yield of free charges ϕ and their mobility $\Sigma\mu$ can be calculated from the maximum ΔG

$$\frac{\Delta G_{max}}{\beta e I_0 F_A} = \varphi\Sigma\mu \quad (2)$$

Here, I_0 is the number of photons per unit area per pulse, β is the ratio of the inner dimensions of the microwave cell, e the elementary charge and F_A the fraction

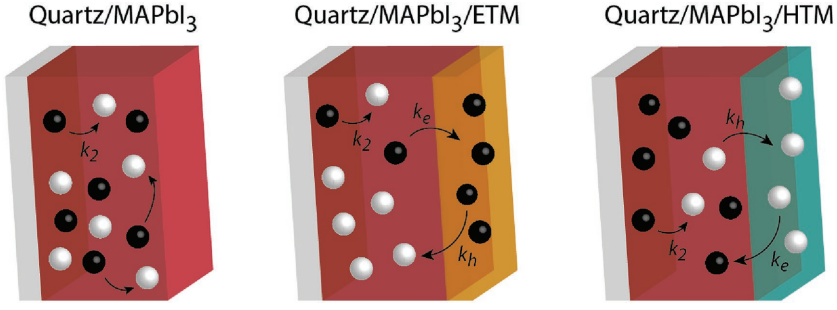

Figure 1. Schematic overview of the sample configurations investigated. Samples are illuminated with a laser pulse through the quartz, generating free electrons (black spheres) and holes (white spheres). In the neat perovskite (left), their concentration will decrease over time due to second-order (k_2) or trap-assisted recombination. In the presence of an electron transport material (ETM, middle), electrons can be extracted (k_e) and recombine with holes via the interface (k_h). Similarly, a hole transport material (HTM, right) extracts the holes (k_h) which can recombine via the interface (k_e) with electrons.

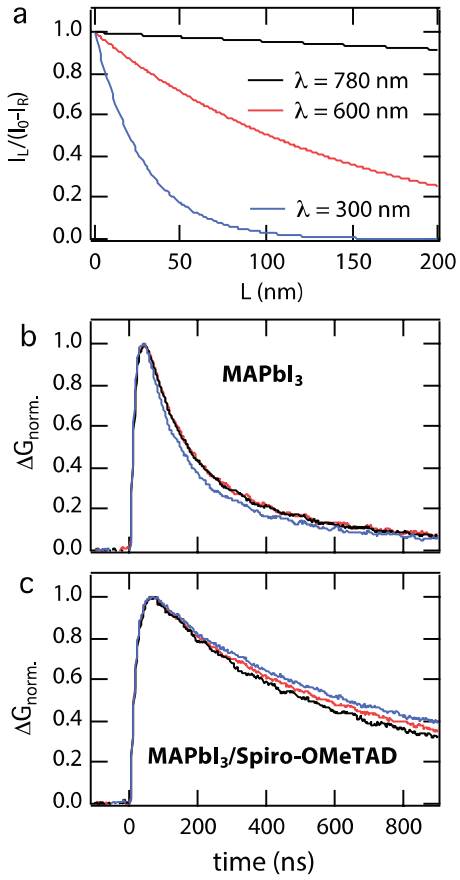

Figure 2. a) Charge carrier generation profile as function of excitation wavelength, calculated using the experimentally determined absorption coefficients (see also Figure S1 in the Supporting Information). b) Normalized time-resolved photoconductance in a thin (≈200 nm) $MAPbI_3$ film and c) in a bilayer of $MAPbI_3$ and Spiro-OMeTAD for a fluence of 10^{10} cm^{-2} absorbed photons (I_0F_A) per pulse at excitation wavelengths of 300, 600, and 780 nm. Since the fraction of absorbed photons (F_A) is wavelength-dependent, the laser intensity I_0 was adjusted in order to obtain the same product of I_0F_A. Hence, the total number of photoexcited charges is similar, however their initial distribution differs (see Figure a). Whereas for $\lambda = 780$ nm, excitation occurs nearly homogeneous throughout the $MAPbI_3$ layer, for $\lambda = 300$ nm charges are generated predominantly ≈150 nm away from the $MAPbI_3$/Spiro-OMeTAD interface.

of light absorbed by the sample at the excitation wavelength. Note that $\Sigma\mu$ is the sum of the electron and hole mobilities ($\mu_e + \mu_h$). Hence, all light-induced mobile charges contribute to the TRMC signal, however scaled by their mobility. Since the electron and hole mobilities in organic compounds are much smaller than in $MAPbI_3$, we can assume that the charges injected into the TM layers do not contribute significantly to ΔG. Thus, the traces in Figure 2c originate from free charges remaining in the perovskite. On comparison of Figure 2b,c, we find that the lifetime of mobile charges is substantially extended in the bilayer configuration with respect to the neat perovskite. We attribute this to injection of holes into the Spiro-OMeTAD, which reduces the probability of electrons remaining in $MAPbI_3$ to recombine with holes and consequently, enhances their lifetime. Interestingly, similar to the neat perovskite, we find that the decay in the bilayer hardly changes with the excitation wavelength. In other words, photogenerated holes can diffuse effectively through the perovskite layer over a distance of at least 150 nm and reach Spiro-OMeTAD. Furthermore, the observation that the electron lifetime in $MAPbI_3$ is shorter in the presence of holes (Figure 2b) confirms our previous conclusions that higher order electron–hole recombination dominates the decay in the neat perovskite.[21] In an effort to investigate whether the observed results can be generalized to $MAPbI_3$ films prepared via different preparation routes, we repeated the experiments with samples spin coated from a stoichiometric precursor solution. We find that, although the absolute charge carrier mobilities and lifetimes are different for the latter, the effect of spin coating the transport layer on top of the spin coated $MAPbI_3$ is the same as observed for the vapor-deposited films (see Figure S6 in the Supporting Information).

To study the electron–hole recombination pathways in more detail, we performed TRMC measurements as function of the initial charge carrier concentration. **Figure 3**a,b shows ΔG normalized for the number of absorbed photons in $MAPbI_3$ (Figure 3a) and $MAPbI_3$/Spiro-OMeTAD (Figure 3b) for charge concentrations ranging from 7×10^{13} to 10^{16} cm^{-3}. In the neat perovskite, the charge carrier decay becomes faster at higher concentrations, which is typical for higher order electron–hole recombination, as discussed previously.[20] Importantly, the opposite trend is observed when holes are transferred to Spiro-OMeTAD: the electron lifetime is shorter at low concentrations and vice versa. In fact, these results suggest the presence of a limited concentration of electron traps. That is, if the concentration of electron traps exceeds the concentration of free electrons, the latter are likely to be immobilized into trap states resulting in a faster decay. On the other hand, if the electron concentration exceeds the trap density, their lifetime will be enhanced, provided that there are no holes to recombine with (Figure 3b). Hence, TRMC measurements using extraction layers enables us to identify the nature of trap states (i.e., electron or hole traps), which is not possible with e.g., photoluminescence measurements. Finally, considering that the signal

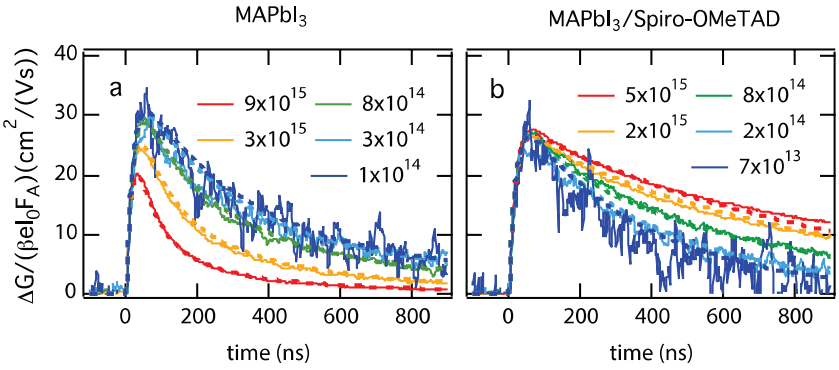

Figure 3. Time-resolved microwave conductivity (TRMC) traces recorded at initial charge carrier densities ranging from 7×10^{13} to 3×10^{16} cm^{-3} ($\lambda = 600$) for a) neat $MAPbI_3$ and b) $MAPbI_3$/Spiro-OMeTAD illuminated through the perovskite.

in Figure 3b originates primarily from electrons remaining in $MAPbI_3$, we can conclude that the contribution of the electrons (μ_e) to the sum of the mobilities $\Sigma\mu$ (Figure 3a) is larger than the contribution of μ_h.

Analogous to our previous work,[20] we use a kinetic model to obtain quantitative information from the intensity-dependent TRMC traces; see **Figure 4**. This model not only includes processes occurring in $MAPbI_3$ (black, see also refs. [20,22]), but is extended to account for the additional pathways introduced by the electron or hole transport material (red).[9] Upon absorption of light ($h\nu$), electrons (n_e) are excited to the conduction band (CB), leaving holes (n_h) in the valence band (VB). The laser pulse (G_C) initially generates equal concentrations of excess electrons ($\Delta n_{CB} = \Delta n_e$) and holes ($-\Delta n_{VB} = \Delta n_h$), which depend on the intensity of absorbed photons. Since the exciton binding energy of several meV is lower than the thermal energy at room temperature,[25] we assume that every absorbed photon yields a single free electron and hole.[26] In $MAPbI_3$, the electrons can recombine with holes via second order recombination (k_2) or traps (k_T and k_R). Additionally, in the presence of an ETM, electrons can be extracted (k_e) and recombine via the interface with holes (k_h). Vice versa, if the TM is hole-selective, $k_h \gg k_e$ and thus k_h represents hole extraction. The time-dependent change in the electron concentrations in the CB, VB, trap states (N_T) and TM are described by the coupled differential Equations (3)–(6), respectively

$$\frac{dn_{CB}}{dt} = \frac{dn_e}{dt} = G_c - k_2 n_e (n_h + p_0) - k_T n_e (N_T - n_T) - k_e n_e \quad (3)$$

$$\frac{dn_{VB}}{dt} = -\frac{dn_h}{dt} = -G_c + k_2 n_e (n_h + p_0) + k_R n_t (n_h + p_0) + k_h n_h \quad (4)$$

$$\frac{dn_t}{dt} = k_T n_e (N_T - n_T) - k_R n_t (n_h + p_0) \quad (5)$$

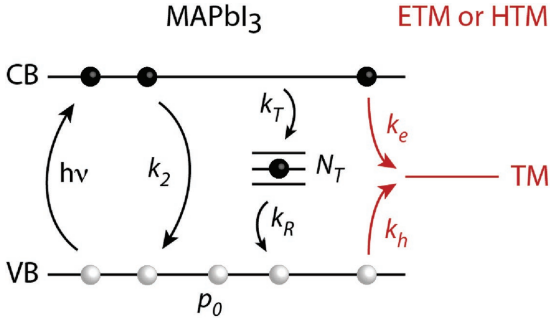

Figure 4. Kinetic model of processes occurring in a bilayer of $MAPbI_3$ perovskite and an organic electron transport material (ETM) or hole transport material (HTM). Electrons (black spheres) and holes (white spheres) are selectively generated in the perovskite film upon absorption of light ($h\nu$) with $\lambda = 600$ nm. In the neat perovskite, electrons can recombine with holes via second order band-to-band recombination (k_2), or get trapped (trap density N_T, trapping rate k_T) and recombine with holes via k_R.[20,22] Both k_2 and k_R are enhanced by the presence of a limited number of dark holes p_0.[27,28] In the presence of an organic transport layer, electrons and holes can be injected via k_e and k_h, respectively, which provides a pathway competitive to recombination in the perovskite.[9] Note that for an ETM, $k_e \gg k_h$ and vice versa.

$$\frac{dn_{TM}}{dt} = k_e n_e - k_h n_h \quad (6)$$

We used the kinetic model shown in Figure 4 to globally fit the experimental TRMC data,[20] which are added as dotted lines in Figure 3a,b. As shown in Figure 3, excellent agreement could be obtained between the modeled and the experimental traces. Remarkably, except for hole injection (k_h), the same kinetic parameters could be used to describe both the neat perovskite and the $MAPbI_3$/Spiro-OMeTAD bilayer (see **Table 1**). Most importantly, the concentration-dependent lifetime of electrons in the absence of holes ($MAPbI_3$/Spiro-OMeTAD, Figure 3b) enables us to accurately determine the trapping parameters N_T and k_T.

Consequently, we find that $k_2 = 2.8 \times 10^{-9}$ cm^3 s^{-1}, $k_T = 6 \times 10^{-9}$ cm^3 s^{-1}, and that the trap density is exceptionally low (3×10^{14} cm^{-3}), similar to spin coated $MAPbI_3$ prepared from $PbCl_2$.[20] The concentration of dark holes (p_0) is 4×10^{14} cm^{-3}, which is in line with experimental findings.[27] Additionally, the only difference between the traces in Figure 3a,b is the injection of holes, from which we deduce that holes are transferred from $MAPbI_3$ to Spiro-OMeTAD with $k_h = 8 \times 10^8$ s^{-1}. As there is no signature of interfacial recombination within the timeframe studied, we conclude that $k_e < 2 \times 10^4$ s^{-1}. In contrast to the present work, we have previously observed little difference between $MAPbI_3$ and $MAPbI_3$/Spiro-OMeTAD.[9] In that work, we proposed that the dark carrier concentration was on the order 10^{16} cm^{-3}, while in the current study this is about two orders of magnitude lower. Consequently, whereas the decay kinetics in $MAPbI_3$/Spiro-OMeTAD were previously dominated by dark carriers, the current data enable for extensive quantitative analysis and accurate extraction of the hole transfer rates.

Whereas we previously had to assume on basis of the effective mass the relative contributions of electrons and holes to the sum of mobilities, these can now be separately determined. Hence, in contrast to previous assumptions, we find that the electron mobility is 30.5 cm^2 V^{-1} s^{-1}, while the hole mobility is 6.5 cm^2 V^{-1} s^{-1}. Considering that the kinetic model also separates the electron and hole lifetimes, the diffusion lengths L_D can now be individually estimated for both charges using $L_D = (D\tau_{1/2})^{1/2}$ with $D = \mu k_B T/e$ and $\tau_{1/2}$ the half lifetime. We estimate that at charge densities comparable to illumination with AM1.5, the electron diffusion length is 1.8 µm, and it is 0.8 µm for the holes. Thus, although the electrons are more mobile than the holes, both diffusion lengths are larger than the ≈0.4 µm $MAPbI_3$ thickness required for sufficient light absorption and thus, both charges are mobile enough to be efficiently collected in a device. Finally, these mobilities corresponding to electron and hole diffusion coefficients of 0.78 and 0.16 cm^2 s^{-1}, respectively, explain the independence of excitation wavelength as presented in Figure 2b,c. That is, it takes approximately 3 ns for the holes to diffuse throughout the 200 nm film, which is below the time response of our measurement.

The above approach enabled us to accurately determine the mobilities and recombination pathways of electrons and holes in $MAPbI_3$, which we used to obtain transfer rates for the other TMs investigated. **Figure 5** shows TRMC traces recorded for bilayers of $MAPbI_3$ and the HTMs: H101 (a) and EDOT-OMeTPA (b), together with the ETMs: PCBM (c), $MAPbI_3$/C60

Table 1. Kinetic parameters for recombination processes in $MAPbI_3$: the exact same parameters were used to describe both the neat perovskite (Figure 3a) and the bilayer systems (Figure 3b and Figure 5).

k_T [$cm^3\ s^{-1}$]	k_2 [$cm^3\ s^{-1}$]	k_R [$cm^3\ s^{-1}$]	N_T [cm^{-3}]	p_0 [cm^{-3}]	μ_e [$cm^2\ V^{-1}\ s^{-1}$]	μ_h [$cm^2\ V^{-1}\ s^{-1}$]
6.0×10^{-9}	2.8×10^{-9}	5.0×10^{-11}	3.0×10^{14}	4.0×10^{14}	30.5 ± 0.5	6.5 ± 0.5

(d), $MAPbI_3$/ICBA (e), and $MAPbI_3$/bis-PCBM (f). The fits to the experimental data as detailed above are added as dotted lines. We note that the perovskite-related mobilities and recombination rates were fixed for all the bilayer systems, leaving k_e and k_h as the only variables. The results are listed in **Table 2**.

Looking at the experimental data for the HTMs investigated, we observe that lifetimes are extended when H101 is spin coated on top of $MAPbI_3$. In contrast to Spiro-OMeTAD however, the decay in $MAPbI_3$/H101 shows higher order recombination effects within the first 100 ns. This suggests that injection into H101 is slower than for Spiro-OMeTAD and therefore, initially in competition with second order recombination in $MAPbI_3$. At longer timescales however, the holes have transferred to H101 and the lifetime of the remaining electrons follows the same trend as for Spiro-OMeTAD. As shown in Figure 5a, this behavior can indeed be modeled using a lower k_h: both the experimental and fitted traces cross over between 100 and 200 ns (see also Figure S7 in the Supporting Information). Additionally, the shorter electron lifetime in $MAPbI_3$/H101 suggests a higher value for interfacial recombination k_e (see Figure 5a and Table 1).

For $MAPbI_3$/EDOT-OMeTPA, as shown in Figure 5b, the decay is substantially faster than in the neat perovskite, i.e., in this bilayer configuration both electrons and holes have recombined within a few nanoseconds. Consequently, we find that holes are transferred with a rate constant of $8 \times 10^8\ s^{-1}$, followed by electron immobilization with $k_e = 1.5 \times 10^8\ s^{-1}$. This rapid quenching of mobile electrons at the $MAPbI_3$/EDOT-OMeTPA interface could be due to recombination with injected holes and/or trapping of electrons at the interface. Similarly, we find that for all the ETMs shown in Figure 5c–f, electron injection is followed by rapid immobilization of holes, as already reported for $MAPbI_3$/PCBM before.[9,29] This is characteristic of the interface between $MAPbI_3$ and all the fullerene-related ETMs studied, since we observed this independently of the $MAPbI_3$ preparation method and the thickness of the ETM (Figure S8a, Supporting Information). Using the kinetic model from Figure 4, we find interfacial recombination rates in the order of 10^6–$10^7\ s^{-1}$. However, we cannot exclude that this represents trapping of holes at the $MAPbI_3$/ETM interface rather than recombination with injected electrons (Figure S8b, Supporting Information). We note that interfacial recombination at the ETM interface is not necessarily a limiting factor for photovoltaic performance, as long as the holes are efficiently collected at the other TM. However, in the case of comparable rate constants for injection and interfacial recombination, as for e.g., EDOT-OMeTPA, this will be detrimental for device performance.

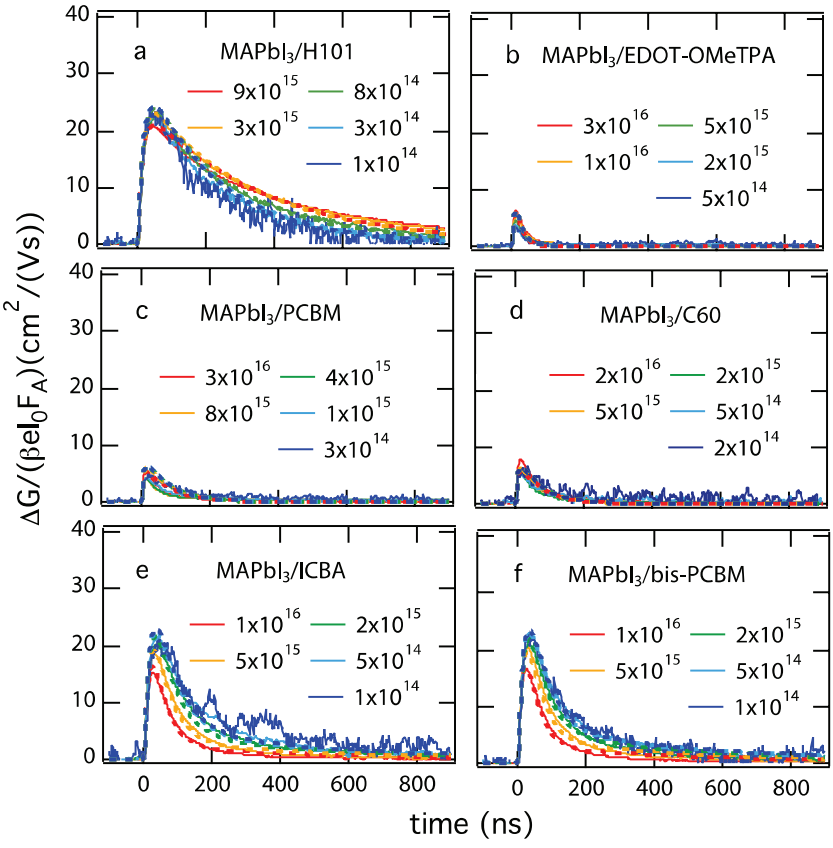

Figure 5. Time-resolved microwave conductivity (TRMC) traces for a) $MAPbI_3$/H101 and b) $MAPbI_3$/EDOT-OMeTPA, c) $MAPbI_3$/PCBM, d) $MAPbI_3$/C60, e) $MAPbI_3$/ICBA, and f) $MAPbI_3$/bis-PCBM recorded at initial charge carrier densities ranging from 10^{14} to $3 \times 10^{16}\ cm^{-3}$ (at $\lambda = 600$). The dotted lines are fit to the experimental data (solid lines), using the model shown in Figure 4 and the kinetic parameters listed in Tables 1 and 2.

Interestingly, comparing the injection rates listed in Table 2, we find that electron transfer from $MAPbI_3$ to ICBA or bis-PCBM is one order of magnitude slower than injection into the other ETMs investigated. This can be understood considering that the lowest unoccupied molecular orbital (LUMO) levels of ICBA and bis-PCBM are located above the CB of $MAPbI_3$, since their electron affinities are 0.2 eV lower than that for PCBM.[30] Although this could result in a higher V_{OC},[19] its band alignment might not favor electron extraction, which explains the relatively low transfer rate in $MAPbI_3$/ICBA. These results suggest that other electron recombination pathways such as trapping or recombination

Table 2. Rate constants for electron (k_e) and hole (k_h) transfer from $MAPbI_3$ to different HTMs and ETMs. Note that for the HTMs, k_h describes extraction and k_e represents interfacial recombination, while the opposite is valid for the ETMs.

	k_h [s^{-1}]	k_e [s^{-1}]
$MAPbI_3$	0	0
$MAPbI_3$/EDOT-OMeTPA	8.0×10^8	1.5×10^8
$MAPbI_3$/Spiro-OMeTAD	4.0×10^8	2.0×10^4
$MAPbI_3$/H101	1.0×10^8	1.8×10^6
$MAPbI_3$/C60	1.2×10^7	3.0×10^8
$MAPbI_3$/PCBM	1.5×10^7	3.0×10^8
$MAPbI_3$/bis-PCBM	1.8×10^6	1.5×10^7
$MAPbI_3$/ICBA	2.0×10^6	1.2×10^7

with holes could be competing with injection into ICBA. That is, if the trapping rate ($\sim k_T N_T$) and/or the higher order recombination rate ($\sim k_2 n_e n_h$) is in excess of the injection rate of (1.2×10^7 s^{-1}), this will dominate over injection. However, in high quality films the trapping rate ($\sim k_T N_T$) is on the order of 10^6 s^{-1} and hence, too small to impede injection.

Using the rate constants for injection as well as the additional recombination pathways in the perovskite, we can now quantify the yield of electron extraction φ_e as function of n_e

$$\varphi_e = \frac{k_e n_e}{k_e n_e + k_2 n_e (n_h + p_0) + k_T n_e (N_T - n_t)} \quad (7)$$

which is defined as the ratio between the electron injection rate and the total recombination rate for electrons. Similarly, the hole extraction yield φ_h is given by

$$\varphi_h = \frac{k_h n_h}{k_h n_h + k_2 n_e (n_h + p_0) + k_R n_t (n_h + p_0)} \quad (8)$$

Figure 6a,b shows φ_e and φ_h, respectively, as function of the excitation density, using the kinetic parameters listed in Tables 1 and 2. Note that AM1.5 illumination under open circuit conditions leads to charge carrier densities on the order of 10^{15} cm^{-3}.[31] Figure 6a shows that at low charge carrier concentrations, φ_e is close to unity for PCBM and C60, which can be understood considering that the injection is fast enough to overcome trapping (i.e., $k_e \gg k_T N_T$). On the other hand, in view of the lower injection rates, electron injection into ICBA and bis-PCBM is in competition both with trapping and second order recombination. Therefore, the transfer yield will always be less than 80% even if all trap-assisted recombination is eliminated (i.e., for $k_e \approx 10^7$ s^{-1} and $k_2 \approx 10^{-9}$ cm^3 s^{-1}). Finally, for all ETMs, φ_e drops down when the concentration increases. This decrease in φ_e is due to second order recombination effects ($\sim k_2 n_e n_h$), which start to dominate over injection at high charge carrier concentrations. The same trends are observed for the HTMs (Figure 6b): φ_h is close to unity at low concentrations and decreases at increasing concentrations. Furthermore, φ_h remains higher for Spiro-OMeTAD than for H101, which can be understood considering that k_h is lower for the latter.

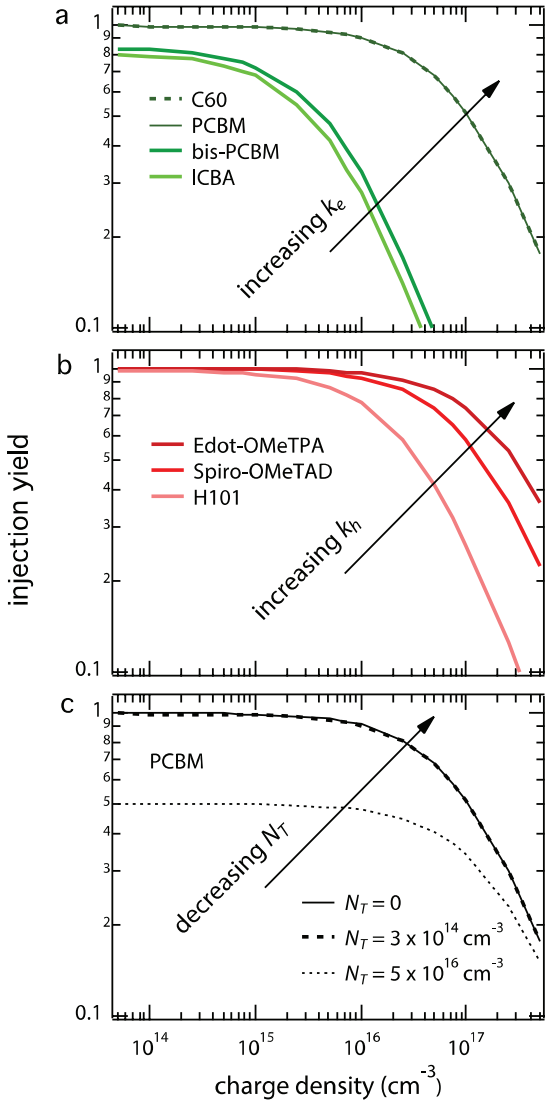

Figure 6. Injection yield as function of charge carrier density for different a) ETMs and b) HTMs, using Equations 7 for the ETMs (a) and 8 for the HTMs (b) and the kinetic parameters from Tables 1 and 2. As we extracted from the TRMC measurements, trapping of electrons ($\sim k_T N_T$) is in competition with extraction (k_e), which can lower the extraction yield. This is especially relevant for ETMs with relatively low injection rates such as ICBA. In general, both φ_e and φ_h decrease when the charge carrier concentration increases (>10^{16} cm^{-3}), since higher order recombination starts to dominate over injection. c) Electron transfer yield from MAPI to PCBM as function of the concentration of electron traps (N_T).

Obviously, electron injection into PCBM could also be impeded by the presence of traps, but only if the trap densities are much higher, e.g., less than 50% of the electrons are injected if N_T would be 5×10^{16} cm^{-3} (see Figure 6c).[20] Similarly, in samples prepared via different routes, the traps could be hole-selective and φ_h could be lower since trapping of holes competes with transfer to the HTM. Finally, considering that illumination with AM1.5 results in charge concentrations in the order of 10^{15}–10^{16} cm^{-3}, these results show that transfer rates to C60, PCBM, EDOT-OMeTPA, and Spiro-OMeTAD are high enough to outcompete second order recombination.

3. Conclusion

In this work, we investigated the transfer of optically excited charge carriers from $MAPbI_3$ to different organic TMs. The TRMC technique was used to study the charge carrier dynamics both in neat $MAPbI_3$ and bilayers of $MAPbI_3$ with an ETM or HTM on top. We proposed a global kinetic model, which we used to quantify the recombination dynamics in the $MAPbI_3$ as well as the additional pathways introduced by the presence of an ETM or HTM. Hence, we were able to deduce rate constants for extraction and interfacial recombination for several organic TMs. Interestingly, we find that both for the state-of-the-art HTM Spiro-OMeTAD and the low-cost alternatives H101 and EDOT-OMeTPA, holes are efficiently collected. However, for the latter this is followed by rapid recombination at the $MAPbI_3$/EDOT-OMeTPA interface, which is expected to limit device performance. For the ETMs, we find that injection into PCBM and C60 is substantially more efficient than into ICBA and bis-PCBM, which might be due to the lower electron affinity of the latter two. Finally, we find that intra-band gap traps do barely affect injection, as long as the trapping rate ($\sim k_T N_T$) is substantially lower than the transfer rates (typically $\approx 10^8$ s^{-1}), which is the case for trap densities less than 10^{15} cm^{-3}.

4. Experimental Section

Sample Preparation: Thin films (200 nm) of $MAPbI_3$ on quartz substrates were prepared by sequential PVD of the precursors lead iodide (PbI_2) and freshly synthesized methylammonium iodide (MAI) (as described elsewhere) in a stoichiometric ratio. Therefore, an adapted evaporation machine (ATC Orion 4-AJA International, Inc.) with deposition controller (SQC-310 Inficon) and thermal evaporation controller (TEC-15A) was used. MAI synthesized using standard procedures and commercially available lead iodide (PbI_2 ≥ 99%, Sigma Aldrich) were put into quartz crucibles, which were positioned in the vacuum chamber after which the pressure was reduced to 10^{-5}–10^{-6} mbar. For each deposition, eight plasma-cleaned quartz substrates were introduced in the vacuum chamber. Consequently, the crucible containing the PbI_2 precursor was heated to 220–240 °C until the desired deposition rate of 0.5 Å s^{-1} was reached, as indicated by a quartz microbalance. The MAI was heated to 60 °C–80 °C to reach a rate of 1.3 Å s^{-1}. Then, $MAPbI_3$ was obtained by alternating deposition of 1 nm PbI_2 and 2 nm MAI (with 16 s in between), which was repeated until a total thickness of 200 nm was reached. Finally, the films were annealed at 100 °C for 1 h. Spin coated MAPI films were prepared from a solution consisting of PbI_2 (1.25 M, TCI chemicals) and MAI (1.25 M, Dyesol) in dimethylformamide (DMF), which was spin coated dynamically (at 5000 rpm, total 15 s) onto the quartz substrate. After 5 s 75 µL of chlorobenzene was added on top of the spinning substrate and afterward the substrates were placed on a hotplate (100 °C for 10 min). The bilayers were prepared by spin coating the HTMs and ETMs on top of the vapor-deposited MAPI films. EDOT-OMeTPA was synthesized according to previously reported procedures,[18] while H101 and Spiro-OMeTAD were obtained from commercial sources. EDOT-OMeTPA was spin coated from a 15 mg mL^{-1} chlorobenzene solution. A 75 mg mL^{-1} chlorobenzene solution was prepared for H101 and Spiro-OMeTAD. Dopants were added to all HTM solutions: 4-*tert*-butylpyridine (t-BP) (10 µL mL^{-1}) and of a lithium bistrifluoromethylsulfonylamine (Li-TFSI) (30 µL mL^{-1}) solution (173 mg mL^{-1} Li-TFSI in acetonitrile solution). While rotating the sample at a speed of 150 rpm, an EDOT-OMeTPA solution (100 µL) was deposited on top of the thin film MAPI, after which the rotational speed was increased to 1200 rpm (45 s). H101 and Spiro-OMeTAD were spincoated by depositing the solution (60 µL) while rotating the sample at 1500 rpm (45 s). This resulted in HTM thicknesses of 40 nm for EDOT-OMeTPA and 250 nm for Spiro and H101.[18] MAPI/HTM bilayers were stored overnight with 30% relative humidity in order to let the HTM oxidize. For the ETMs, PCBM, bis-PCBM, and ICBA, ETM/chlorobenzene (35 mg mL^{-1}) solutions were prepared. From these solutions, 60 µL was deposited on the sample while rotating at 3000 rpm (45 s). The thickness of the PCBM layer was found to be around 70 nm. Layers of the other ETMs were estimated to have similar thickness.

Optical Characterization: Absorption and transmission spectra were recorded with a Perkin-Elmer Lambda 1050 spectrophotometer equipped with an integrated sphere. The thin films were placed in front of the sphere to measure the fraction of transmitted light (F_T) and under an angle of 10° inside the sphere to detect the total fraction of reflected and transmitted photons (F_{R+T}). From here, the authors calculated the fraction of absorbed light (F_A)

$$F_A = 1 - F_{T+R} \tag{9}$$

The fraction of reflected light (F_R) was determined from

$$F_R = 1 - F_A - F_T \tag{10}$$

The absorption coefficient α is often calculated from the transmission spectrum using

$$\frac{I_L}{I_0} = e^{-\alpha L} \tag{11}$$

where I_L/I_0 equals F_T for a sample of thickness L with negligible reflection. However, since $MAPbI_3$ films are highly reflective, α was obtained from

$$\frac{F_T}{1 - F_R} = e^{-\alpha L} \tag{12}$$

Photoconductance Measurements: The thin films on quartz substrates were placed in a sealed resonance cavity inside an N_2-filled glovebox. The TRMC technique was used to measure the change in microwave (8–9 GHz) power after pulsed excitation (repetition rate 10 Hz) of the samples at different excitation wavelengths.[24] The bilayers were illuminated both from the front side (through the electrode) and the back side (through the quartz). Neutral density filters were used to vary the intensity of the incident light. The photo-excitation-induced change in microwave power is related to the change in conductance ΔG by a sensitivity factor K (Equation (1)). The rise of ΔG is limited by the width of the laser pulse (3.5 ns FWHM) and the response time of the microwave system (18 ns). The slow repetition rate of the laser of 10 Hz ensures full relaxation of all photo-induced charges to the ground state before the next laser pulse hits the sample. Before and during the photoconductance measurements, the samples were not exposed to moisture and air to prevent degradation.

Supporting Information

Supporting Information is available from the Wiley Online Library or from the author.

Acknowledgements

This work was supported by the Netherlands Organization for Scientific Research (NWO) under the Echo grant number: 712.014.007. Andreas Baumann and Philipp Rieder are acknowledged for technical support.

The authors thank Davide Bartesaghi for critical reading of this manuscript.

Received: October 24, 2016
Revised: December 6, 2016
Published online: February 17, 2017

[1] A. Kojima, K. Teshima, Y. Shirai, T. Miyasaka, *J. Am. Chem. Soc.* **2009**, *131*, 6050.
[2] S. D. Stranks, G. E. Eperon, G. Grancini, C. Menelaou, M. J. P. Alcocer, T. Leijtens, L. M. Herz, A. Petrozza, H. J. Snaith, *Science* **2013**, *342*, 341.
[3] http://www.nrel.gov, accessed: October, 2016.
[4] B. Wu, K. Fu, N. Yantara, G. Xing, S. Sun, T. C. Sum, N. Mathews, *Adv. Energy Mater.* **2015**, *5*, 1500829.
[5] P. Calado, A. M. Telford, D. Bryant, X. Li, J. Nelson, B. C. O'Regan, P. R. F. Barnes, *Nat. Commun.* **2016**, *7*, 13831.
[6] T. M. Brenner, D. A. Egger, L. Kronik, G. Hodes, D. Cahen, *Nat. Rev. Mater.* **2016**, *1*, 15007.
[7] J. S. Manser, J. A. Christians, P. V Kamat, *Chem. Rev.* **2016**, *116*, 12956.
[8] K. Pydzińska, J. Karolczak, I. Kosta, R. Tena-Zaera, A. Todinova, J. Idígoras, J. A. Anta, M. Ziółek, *ChemSusChem* **2016**, *9*, 1647.
[9] C. S. Ponseca Jr., E. M. Hutter, P. Piatkowski, B. Cohen, T. Pascher, A. Douhal, A. Yartsev, V. Sundström, T. J. Savenije, *J. Am. Chem. Soc.* **2015**, *137*, 16043.
[10] S. Makuta, M. Liu, M. Endo, H. Nishimura, A. Wakamiya, Y. Tachibana, *Chem. Commun.* **2015**, *52*, 673.
[11] P. Piatkowski, B. Cohen, F. J. Ramos, M. Di Nunzio, M. K. Nazeeruddin, M. Grätzel, S. Ahmad, A. Douhal, *Phys. Chem. Chem. Phys.* **2015**, *17*, 14674.
[12] J. C. Brauer, Y. H. Lee, M. K. Nazeeruddin, N. Banerji, *J. Mater. Chem. C* **2016**, *4*, 5922.
[13] N. Ishida, A. Wakamiya, A. Saeki, *ACS Photonics* **2016**, *3*, 1678.
[14] O. Malinkiewicz, A. Yella, Y. H. Lee, G. M. Espallargas, M. Graetzel, M. K. Nazeeruddin, H. J. Bolink, *Nat. Photonics* **2013**, *8*, 128.
[15] M. Liu, M. B. Johnston, H. J. Snaith, *Nature* **2013**, *501*, 395.
[16] C. Momblona, L. Gil-Escrig, E. Bandiello, E. M. Hutter, M. Sessolo, K. Lederer, J. Blochwitz-Nimoth, H. J. Bolink, *Energy Environ. Sci.* **2016**, *9*, 3456.
[17] H. Li, K. Fu, A. Hagfeldt, M. Grätzel, S. G. Mhaisalkar, A. C. Grimsdale, *Angew. Chem., Int. Ed.* **2014**, *53*, 4085.
[18] M. L. Petrus, T. Bein, T. J. Dingemans, P. Docampo, *J. Mater. Chem. A* **2015**, *3*, 12159.
[19] J. Y. Jeng, Y. F. Chiang, M. H. Lee, S. R. Peng, T. F. Guo, P. Chen, T. C. Wen, *Adv. Mater.* **2013**, *25*, 3727.
[20] E. M. Hutter, G. E. Eperon, S. D. Stranks, T. J. Savenije, *J. Phys. Chem. Lett.* **2015**, *6*, 3082.
[21] E. M. Hutter, M. C. Gélvez-Rueda, A. Osherov, V. Bulović, F. C. Grozema, S. D. Stranks, T. J. Savenije, *Nat. Mater.* **2017**, *16*, 115.
[22] S. D. Stranks, V. M. Burlakov, T. Leijtens, J. M. Ball, A. Goriely, H. J. Snaith, *Phys. Rev. Appl.* **2014**, *2*, 34007.
[23] G.-J. A. H. Wetzelaer, M. Scheepers, A. M. Sempere, C. Momblona, J. Avila, H. J. Bolink, *Adv. Mater.* **2015**, *27*, 1837.
[24] T. J. Savenije, A. J. Ferguson, N. Kopidakis, G. Rumbles, *J. Phys. Chem. C* **2013**, *117*, 24085.
[25] A. Miyata, A. Mitioglu, P. Plochocka, O. Portugall, J. T.-W. Wang, S. D. Stranks, H. J. Snaith, R. J. Nicholas, *Nat. Phys.* **2015**, *11*, 582.
[26] V. D'Innocenzo, G. Grancini, M. J. P. Alcocer, A. R. S. Kandada, S. D. Stranks, M. M. Lee, G. Lanzani, H. J. Snaith, A. Petrozza, *Nat. Commun.* **2014**, *5*, 3586.
[27] C. Bi, Y. Shao, Y. Yuan, Z. Xiao, C. Wang, Y. Gao, J. Huang, *J. Mater. Chem. A* **2014**, *2*, 18508.
[28] Q. Wang, Y. Shao, H. Xie, L. Lyu, X. Liu, Y. Gao, J. Huang, *Appl. Phys. Lett.* **2014**, *105*, 15.
[29] K. Wojciechowski, S. D. Stranks, A. Abate, G. Sadoughi, A. Sadhanala, N. Kopidakis, G. Rumbles, C.-Z. Li, R. H. Friend, A. K.-Y. Jen, H. J. Snaith, *ACS Nano* **2014**, *8*, 12701.
[30] C.-G. Wu, C.-H. Chiang, S. H. Chang, *Nanoscale* **2016**, *8*, 4077.
[31] M. B. Johnston, L. M. Herz, *Acc. Chem. Res.* **2016**, *49*, 146.